Journal of Power Sources 194 (2009) 349–359

Contents lists available at ScienceDirect

Journal of Power Sources

journal homepage: www.elsevier.com/locate/jpowsour

Numerical analysis of effects of flow channel size on reactant transport in a proton exchange membrane fuel cell stack

Chin-Hsiang Cheng[a,*], Hung-Hsiang Lin[b]

[a] Department of Aeronautics and Astronautics, National Cheng Kung University, No.1, Ta Shieh Road, Tainan, 70101 Taiwan, ROC
[b] Institute of Nuclear Energy Research, Lungtan, 32546 Taiwan, ROC

ARTICLE INFO

Article history:
Received 23 March 2009
Received in revised form 21 April 2009
Accepted 21 April 2009
Available online 7 May 2009

Keywords:
Stack
Proton exchange membrane fuel cell
Numerical simulation
Experiment
Channel design

ABSTRACT

Numerical simulation of transport phenomena in a six-cell PEM fuel cell stack is performed to adjust the gas channel size of individual cells to obtain evenly distributed cell voltages. Commercial software, CFD-ACE+, is used as the solution code, and the effects of various combinations of geometric parameters of the channels are investigated, including the channel width ratios (Λ) and the heights of the gas channels (h). Furthermore, a six-cell fuel cell stack was assembled for experiments, and the polarization curves of the stack were measured. With the help of the experimental data, the values of the physical and electrochemical parameters adopted in the computation model are determined, and the computation model is then used in numerical simulation. Under the assumption of no dry out in the cells, an even voltage distribution can be obtained if the distribution of reactant gas is uniform among the cells. In this study, better combinations of the channel width ratios and the heights of gas channels for individual cells are proposed to yield a uniform distribution of the reactant gases in the cells. An adjustment of the geometric parameters of gas channels that leads to evenly distributed voltages is attempted, and a 16.5% increase in the performance of the fuel cell stack is observed simply by adjusting the sizes of the gas channels.

1. Introduction

A single-cell proton exchange membrane fuel cell (PEMFC) is equipped with a polymer electrolyte membrane, which is sandwiched between two electrodes with two gas diffusion layers to form a membrane-electrode assembly (MEA). In a typical fuel cell structure [1], the MEA is placed between two carbon plates with machined groves on the inner faces that are used as flow channels to provide sufficient amount of fuel and oxidant. Hydrogen gas is supplied as a fuel to the flow channels facing the gas diffusion layer at the anode side, and oxygen gas, or air, is supplied to the flow channels facing the gas diffusion layer at the cathode side. Both the anode and the cathode sides contain a catalyst to speed up the electro-chemical reaction processes. The fuel is oxidized on the anode side, and free electrons are conducted through the load in an external circuit to the cathode side. The polymer electrolyte membrane prevents fuel and oxidant molecules from mixing, and, therefore, it prevents direct combustion. However, the ions are allowed to migrate through the polymer electrolyte membrane toward the cathode side where the oxidant and the electrons are provided. The electro-chemical reaction at the cathode side produces water and completes the circuit.

A number of theoretical studies have considered modeling the electrochemical reaction and transport phenomena in a single-cell PEMFC. For example, a three-dimensional numerical analysis of a straight channel in a PEM fuel cell was performed by Dutta et al. [2] using commercial computational fluid dynamics software. The authors found that membrane thickness, cell voltage and current density can affect water transport across the membrane. Hu et al. [3] reported a numerical signal phase model that includes a three-dimensional solution to the fluid flow, species transport and electrochemical reaction in PEM fuel cells with a conventional and an interdigitated flow field. They found that the interdigitated flow field has better performance because of its advantage in mass-transport ability; however, it has a larger pressure loss for its flow through the electrode. You and Liu [4] considered liquid water accumulation in the straight channels on the cathode side and used a multi-phase model to obtain the simulation results. Recently, Lin and coworkers [5,6] investigated optimization of the proton exchange membrane fuel cell based on a three-dimensional numerical model. Optimization methods were introduced into the model to determine the optimal combination of the design parameters, including the channel width ratio, the porosity of gas diffusion layer (GDL), and the porosity of the catalyst layer.

* Corresponding author. Tel.: +886 6 2757575x63627; fax: +886 6 2389940.
E-mail address: chcheng@mail.ncku.edu.tw (C.-H. Cheng).

0378-7753/$ – see front matter © 2009 Elsevier B.V. All rights reserved.
doi:10.1016/j.jpowsour.2009.04.075

Nomenclature

a	water activity
D	mass diffusivity ($m^2\ s^{-1}$)
F	Faraday constant (96,487 C mol^{-1})
h	height of gas channel (m)
i	local electric current density (A m^{-3})
$\bar{i}$	local ionic current density (A m^{-3})
I	electric current density (A m^{-2})
j	transfer current density (A m^{-3})
k	permeability (m^2)
l_C	gas channel width (m)
l_L	gas channel length (m)
l_P	width of a module (m)
M	molecular weight (kg $kmol^{-1}$)
n	coordinate in the direction normal to the surface
P	pressure (Pa)
P	power density (W m^{-2})
r	concentration parameter
R	universal gas constant (8.314 J mol^{-1} K^{-1})
S	source term in species equation
T	temperature (K)
t	thickness (m)
$\vec{U}$	gas velocity vector (m s^{-1})
v	gas velocity (m s^{-1})
V	voltage (V)
υ_N	volume occupied by Nafion in catalyst layer (m^3)
υ_S	volume occupied by solid catalyst particles in catalyst layer (m^3)
υ_t	total volume of catalyst layer (m^3)
υ_V	volume of void space in catalyst layer (m^3)
Y	mass fraction
X	mole fraction
x, y, z	Cartesian coordinates

Greek Symbols

α	charge transfer coefficient for the reaction
χ	Bruggemann coefficient
ε_{GDL}	porosity of gas diffusion layer
$\varepsilon_{N,Cat}$	volume fraction of Nafion in catalyst layer
$\varepsilon_{S,Cat}$	volume fraction of solid catalyst particles in catalyst layer
$\varepsilon_{V,Cat}$	volume fraction of void space in catalyst layer
ϕ	electric potential (V)
φ	phase potential (V)
Λ	gas channel width ratio (l_C/l_P)
λ	membrane water content (kmol H_2O(kmol SO_3^-)$^{-1}$)
ρ	density of gas (kg m^{-3})
σ	electronic conductivity of solid catalyst particle (Ω^{-1} m^{-1})
Γ	ionic conductivity (Ω^{-1} m^{-1})
τ	fluid stress (N m^{-2})
ζ	source term in electronic conduction equation

Superscripts

eff	effective

Subscripts

a	anode
b	bottom
c	cathode/gas channel
Cat	catalyst layer
GDL	gas diffusion layer
in	inlet
m	membrane
N	Nafion
P	carbon plate
out	outlet
ref	reference
S	solid catalyst particles
t	top
1–6	Cell 1–Cell 6

However, in general, the voltage produced by a single-cell fuel cell only ranges from 0.65 to 1.0 V. For practical applications, a number of cells must be assembled in series to construct a fuel cell stack. The number of unit cells required in a stack depends on the desired voltage or the net power capacity, which can vary from less than 100 W for portable power generators to around 300 kW for heavy vehicles [7]. Recently, significant progress in the development of PEMFC stack technology has been achieved by an increasing number of experimental [8–11] and theoretical [12–16] studies.

When designing a fuel cell stack, one needs be able to measure individual cell voltages. In an ideal situation, all unit cells are identical, and there are no performance differences between the cells. In reality, cell performances differ, sometimes drastically, due to unequal reactant supply. In practice, non-evenly distributed cell voltages among the unit cells may cause a great reduction in the power output of the stack. To achieve an even voltage distribution, the stack should be operated on the premise that the reactant gases are distributed uniformly to all unit cells of the stack. Since both the fuel and the oxidant gases are fed to the anode and the cathode sides, respectively, of all unit cells of the stack through a manifold and the flow channel network, the design of the manifold and the flow channel network is regarded as one of the critical issues related to stack performance. Karimi et al. [17] found that the stack performance is considerably affected by the size and the number of flow channels on bipolar plates. To achieve improved stack performance, the stack manifold, flow channels on the bipolar plates, and the stack operating conditions should be designed carefully. Mohamed and Jenkins [12] presented an approach based on the genetic algorithm technique to find the optimal configuration of the stack in terms of the number of cells and cell surface area. Pan et al. [18] carried out an optimal design of complex manifold geometries for uniform flow distribution between microchannels by means of the flow network method. Tonomura et al. [19] performed a CFD-based optimal design of a manifold in plate-fin microdevices.

In the present study, numerical methods are employed to investigate the dependence of the performance of a six-cell PEMFC stack on the geometric design of the gas channels in the individual cells. Adjustment for the channel width ratios (Λ) or the heights of gas channels (h) of the cells has been attempted to obtain evenly distributed cell voltages. In the meantime, a six-cell fuel cell stack (190 W) has been assembled for experiments, and the polarization curves of the stack have been adopted to verify the validity of the numerical solutions.

2. Theoretical model

The physical model of a stack consisting of six unit cells, each of which is equipped with parallel straight channels on both the anode and the cathode carbon plates, is shown in Fig. 1. There are several advantages associated with the straight channels. For example, compared to the serpentine channels, where there may be eddies near bends in the channel, straight channels provide fewer places for water to accumulate in the channels. Another advantage is that there is a smaller pressure drop with fluids flowing in the channels

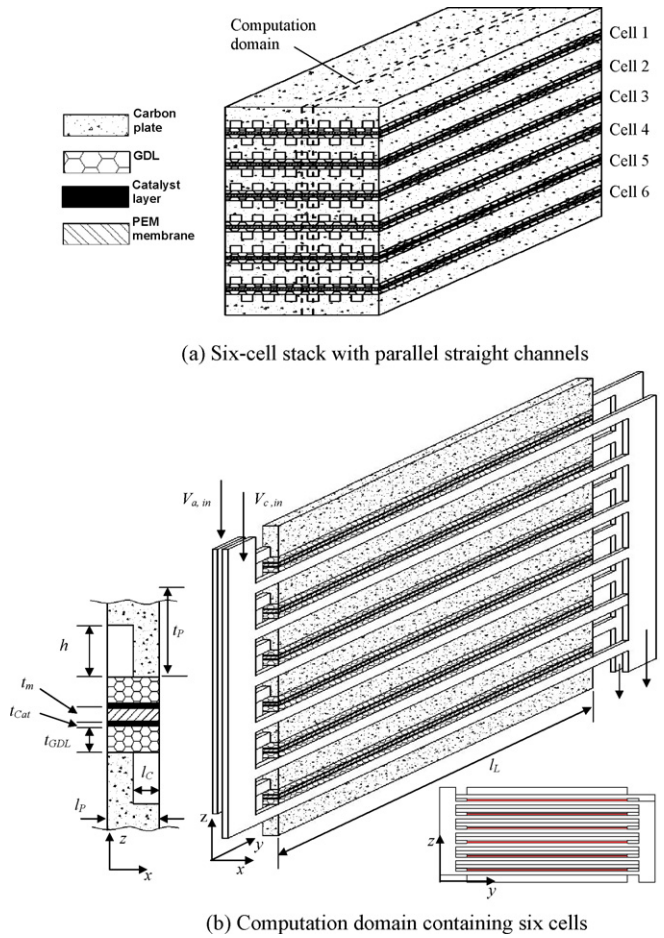

Fig. 1. Schematic of a six-cell proton exchange membrane fuel cell stack. (a) Six-cell stack with parallel straight channels. (b) Computation domain containing six cells.

since there are no corners. Furthermore, plates with straight parallel channel flow fields may be easier to manufacture than those with more complex shapes. Fig. 1(a) illustrates a schematic of the stack with the cells numbered from 1 to 6, and Fig. 1(b) conveys the computation domain of the solution module, which covers a half channel area for the six cells and the inlet/outlet manifolds. For the pattern of straight parallel channels considered, if the number of gas channels is sufficiently large, a periodic transport phenomenon is expected to develop from channel to channel for all the cells. Thus, one only needs to deal with the computation domain indicated by the dashed lines, and the right and the left faces (y–z planes at $x = 0$ and $x = l_P$) of the computation domain are the symmetric planes. Here, the origin of the Cartesian coordinate is put at the bottom left corner of the computation domain where the y-direction represents the streamwise direction of the channels. The reactant gases, hydrogen and air, are delivered into the cells through the inlet manifolds, and the product gases exit through the outlet manifolds after the reaction. For each cell, the gas channels on the anode side and those on the cathode side are placed in a staggered arrangement. The width of the solution domain is denoted with l_P, and the half channel width is l_C; therefore, the channel has width ratio (Λ) defined as l_C/l_P. The channel width and channel height (h) are regarded as two major geometric parameters to elevate the performance of the stack. The values of the fixed parameters are listed in Table 1. The existing information for the values of these fixed parameters is scattered. However, the parameters are chosen based on a review of the existing information [1–6]. Note that in this study, the operating temperature and pressure are assigned to be 343 K and 101,325 Pa, respectively. The value of the operating voltage of the fuel cell stack is varied between 3.5 and 5.75 V in the computation.

Table 1
Fixed parameters.

Parameter	Symbol	Value
Operating temperature, K	T	343
Operating pressure, Pa	P	101,325
Operating stack voltage, V	V	3.5–5.75
Gas channel length, m	l_L	5.0×10^{-2}
Width of a solution module, m	l_P	1.0×10^{-3}
Thickness of catalyst layer, m	t_{Cat}	3.0×10^{-5}
Thickness of carbon plate, m	t_P	3.0×10^{-3}
Thickness of gas diffusion layer, m	t_{GDL}	3.0×10^{-4}
Thickness of membrane, m	t_m	1.76×10^{-4}
Bruggemann coefficient of gas diffusion layer	χ_{GDL}	1.5
Bruggemann coefficient of catalyst layer	χ_{Cat}	1.5
GDL permeability, m^2	k_{GDL}	1.76×10^{-11}
Catalyst layer permeability, m^2	k_{Cat}	1.76×10^{-11}
Anode inlet hydrogen velocity, m s^{-1}	$v_{a,in}$	0.1667
Cathode inlet air velocity, m s^{-1}	$v_{c,in}$	0.5
Anode inlet mass fraction of H_2	$Y_{H_2,i}$	0.2
Anode inlet mass fraction of H_2O	$Y_{H_2O,i}$	0.8
Cathode inlet mass fraction of O_2	$Y_{O_2,i}$	0.174
Cathode inlet mass fraction of N_2	$Y_{N_2,i}$	0.609
Cathode inlet mass fraction of H_2O	$Y_{H_2O,i}$	0.217
Anode concentration parameter	r_a	1.0
Cathode concentration parameter	r_c	1.0
Anodic charge transfer coefficients for anode reaction	$\alpha_{a,a}$	0.5
Cathodic charge transfer coefficients for anode reaction	$\alpha_{a,c}$	0.5
Aanodic charge transfer coefficients for cathode reaction	$\alpha_{c,a}$	1.5
Cathodic charge transfer coefficients for cathode reaction	$\alpha_{c,c}$	1.5
Reference transfer current density at anode, A m^{-3}	$j_{a,ref}$	4.5×10^9
Reference transfer current density at cathode, A m^{-3}	$j_{c,ref}$	250
Volume fraction of Nafion in catalyst layer	$\varepsilon_{N,Cat}$	0.3
Volume fraction of void space in catalyst layer	$\varepsilon_{V,Cat}$	0.112
Volume fraction of solid catalyst particles in catalyst layer	$\varepsilon_{S,Cat}$	0.588
Porosity of gas diffusion layer	ε_{GDL}	0.5
Effective ionic conductivity of catalyst layer, Ω^{-1} m^{-1}	Γ_{Cat}^{eff}	4.2
Ionic conductivity of Nafion, Ω^{-1} m^{-1}	$\Gamma_{N,Cat}$	25.56
Effective mass diffusivity of oxygen in catalyst layer, cm^2 s^{-1}	$D_{O_2,Cat}^{eff}$	1.9546×10^{-3}
Effective mass diffusivity of hydrogen in catalyst layer, cm^2 s^{-1}	$D_{H_2,Cat}^{eff}$	0.985×10^{-3}
Effective mass diffusivity of oxygen in GDL, cm^2 s^{-1}	$D_{O_2,GDL}^{eff}$	1.845×10^{-2}
Effective mass diffusivity of hydrogen in GDL, cm^2 s^{-1}	$D_{H_2,GDL}^{eff}$	0.930×10^{-2}
Electronic conductivity of gas diffusion layer, Ω^{-1} m^{-1}	σ_{GDL}	150
Electronic conductivity of carbon plate, Ω^{-1} m^{-1}	σ_P	4000
Electronic conductivity of catalyst layer, Ω^{-1} m^{-1}	$\sigma_{S,Cat}$	1414

The theoretical model is developed under the following simplifications and assumptions:

1. Compression pressure is applied by fastening the bolts that clamp the cells of the stack tightly, and, therefore, at the interfaces between the layers of any cells, there is no appreciable contact resistance against the conduction of heat, electrons, or ions.
2. For all the cells, the gas flows in the gas channels, the porous layers are laminar and compressible, and the effects of buoyancy on the flow motion are ignored.
3. The gas diffusion layers and the catalyst layers are homogeneous, isotropic porous media.

4. Inlet and outlet conditions and thermodynamic and electrochemical properties of the gases and the solid materials of the stack components are assumed to be constant.
5. Water exists in the entire fuel cell only in the vapor phase, and no phase change process is taken into consideration.
6. The operating temperature is uniform and constant in the stack.
7. Because of the high ohmic resistance of the membrane, the interface between the catalyst layer and the membrane is assumed to be insulated against electrons.
8. The fuel cell stack is operated under steady conditions.

The present three-dimensional model involves electrochemical reactions; mass, momentum, and species transport phenomena; ionic conduction; electronic conduction; and Nafion loading effects. The modeling proposed by Cheng et al. [5] that was applied for a single-cell system is extended to the analysis of the six-cell stack. The governing equations of the theoretical model are described briefly in the following.

2.1. Electrochemical reactions (catalyst layers)

Note that for each cell, H_2 and O_2 are consumed by the reactions in the catalyst layers of the anode and cathode sides, respectively, and H_2O is the product of the reaction at the cathode sides. The source terms for different species are

$$S_{H_2} = -\frac{j_a}{2F} \tag{1a}$$

$$S_{O_2} = \frac{j_c}{4F} \tag{1b}$$

$$S_{H_2O} = -\frac{j_c}{2F} \tag{1c}$$

where j_a and j_c are the transfer current densities at the anode and the cathode, respectively, which are calculated based on the Butler–Volmer condition:

$$j_a = j_{a,ref}\left(\frac{Y_{H_2}}{Y_{H_2,ref}}\right)^{r_a} \times \left[\exp\left\{\frac{\alpha_{a,a}F}{RT}\eta\right\} - \exp\left\{\frac{-\alpha_{a,c}F}{RT}\eta\right\}\right] \tag{2a}$$

$$j_c = j_{c,ref}\left(\frac{Y_{O_2}}{Y_{O_2,ref}}\right)^{r_a} \times \left[\exp\left\{\frac{\alpha_{c,a}F}{RT}\eta\right\} - \exp\left\{\frac{-\alpha_{c,c}F}{RT}\eta\right\}\right] \tag{2b}$$

where $j_{a,ref}$ and $j_{c,ref}$ are the reference transfer current densities, and r_a and r_c the concentration parameters, at the anode and the cathode, respectively. In addition, $\alpha_{a,a}$ and $\alpha_{a,c}$ are the anodic and the cathodic charge transfer coefficients for anode reaction, and $\alpha_{c,a}$, and $\alpha_{c,c}$ the anodic and the cathodic charge transfer coefficients for cathode reaction. Furthermore, $Y_{O_2,ref}$ and $Y_{H_2,ref}$ are the reference concentrations at which the exchange current densities were obtained. All the reference values of these coefficients are given in Table 1.

2.2. Mass, momentum, and species transport (gas channels, GDLs, and catalyst layers)

The flow channels and the gas diffusion layers in the cells are employed to deliver the reactant gases uniformly into the catalyst layers for reactions. The governing equations to predict the mass, momentum, and species transport phenomena in the gas channels, GDLs, and catalyst layers can be expressed, in general form, in accordance with the conservation laws in mass, momentum, and species. In the porous medium layers, the equations are derived based on the non-Darcy law.

Mass conservation:

$$\nabla\cdot(\varepsilon\rho\vec{U}) = 0 \tag{3}$$

Momentum conservation:

$$\nabla\cdot(\varepsilon\rho\vec{U}\vec{U}) = -\varepsilon\nabla P + \nabla\cdot(\varepsilon\tau) + \frac{(\varepsilon)^2\mu\vec{U}}{k} \tag{4}$$

Species equation:

$$\nabla\cdot(\varepsilon\rho U Y_i) = \nabla\cdot(D_i^{eff}\nabla Y_i) + S_i \tag{5}$$

where ε and k are the porosity and the permeability of the porous layers, respectively; τ represents the fluid stress tensor. Fuel gas at the anode contains H_2 and H_2O, and oxidant gas; the cathode contains O_2, N_2, and H_2O. Y_i denotes the species mass fraction of species i. Note that for pure fluid flows in the gas channels, the values of ε and k are $\varepsilon = 1$ and $k = \infty$.

In Eq. (5), the term S_i standing for the source term of species i is calculated by Eq. (1), and the calculation for the effective mass diffusivity of species i (D_i^{eff}) is based on Bruggemann's equation, that is,

$$D_i^{eff} = (\varepsilon)^{\chi} D_i \tag{6}$$

where D_i is the mass diffusivity of species i, and χ is the Bruggemann coefficient of the porous layer.

2.3. Ionic conduction (catalyst layers and proton exchange membranes)

Ionic conduction occurs in the catalyst layers and the proton exchange membrane. The ionic conduction equation for determination of the phase potential (φ) in the catalyst layers is

$$-\nabla\cdot(\Gamma_{Cat}^{eff}\nabla\varphi_{Cat}) = \zeta \tag{7}$$

where φ_{Cat} is the phase potential and Γ_{Cat}^{eff} is the effective ionic conductivity of the catalyst layers. The effective ionic conductivity Γ_{Cat}^{eff} is evaluated by using

$$\Gamma_{Cat}^{eff} = \varepsilon_{N,Cat}^{\chi_{Cat}}\Gamma_{N,Cat} \tag{8}$$

In addition, for the catalyst layers, the source term of Eq. (7), ζ, is equal to the transfer current densities $-j_a$ and j_c for the anode and the cathode, respectively, which are calculated with Eqs. (2a) and (2b).

On the other hand, the ionic conduction equation for the proton exchange membrane is expressed as

$$\nabla\cdot(\Gamma_m\nabla\varphi_m) = 0 \tag{9}$$

where φ_m is the phase potential and Γ_m is the ionic conductivity of the membrane, which can be determined by the relation proposed by Springer et al. [20] as

$$\Gamma_m(T) = \exp\left[1268\left(\frac{1}{303} - \frac{1}{T}\right)\right](0.005239\lambda - 0.00326) \tag{10}$$

where the water content of the membrane (λ) is dependent on a dimensionless water activity in the membrane (a) according to experimental data. The activity is defined as

$$a = \frac{X_{H_2O}P}{P_{sat}} \tag{11}$$

where the saturation pressure of water vapor can be computed from

$$\log_{10}P_{sat} = -2.1794 + 0.02953(T - 273.15) - 9.1837 \times 10^{-5}(T - 273.15)^2 + 1.4454 \times 10^{-7}(T - 273.15)^3 \tag{12}$$

with T in K. The correlation between λ and a is derived as

$$\lambda = \begin{cases} 0.043 + 17.81a - 39.85a^2 + 36a^3 & 0 \le a \le 1 \\ 14 + 1.4(a-1) & 1 < a \le 3 \end{cases} \quad (13)$$

Based on the solutions for the phase potential (φ), the distribution of local ionic current density ($\vec{i}$) in the catalyst layers and the proton exchange membrane may be further determined with $\vec{i} = -\Gamma\nabla\varphi$.

2.4. Electronic conduction (carbon plates, GDLs, and catalyst layers)

The carbon plate, the GDL, and the catalyst layers all serve as conductors for electric current. In the carbon plate and the GDL, there is no electrochemical reaction taking place. The electrochemical reactions only take place in the catalyst layers. Therefore, in these three components, the electronic conduction equation may be expressed in general form as

$$\nabla \cdot (\sigma^{eff}\nabla\phi) = \zeta \quad (14)$$

where ϕ is the electronic potential and σ^{eff} denotes the effective electronic conductivity. For the carbon plates, the effective electronic conductivity σ^{eff} is treated as a constant (σ_P). For the porous gas diffusion and catalyst layers, the magnitude of the effective electronic conductivity is determined in terms of the porosity in accordance with the Bruggemann's equation as

$$\sigma^{eff}_{GDL} = (1-\varepsilon_{GDL})^{\chi_{GDL}}\sigma_{GDL} \quad (15a)$$

$$\sigma^{eff}_{Cat} = \varepsilon^{\chi_{Cat}}_{S,Cat}\sigma_{S,Cat} \quad (15b)$$

It is noticed that the effective electronic conductivity of the catalyst layer (σ^{eff}_{Cat}) increases with the volume fraction of solid catalyst particles in the catalyst layer ($\varepsilon_{S,Cat}$). Also, note that, for the catalyst layers, the source term ζ is identical to that of Eq. (7), whereas for the carbon plates or the GDL, the source term, ζ, is zero for without an electrochemical reaction.

2.5. Nafion loading (catalyst layers)

When Nafion is introduced into the catalyst layer, it reduces the electronic conductivity of the catalyst layer. However, since it is a good conductor for the hydrogen protons, Nafion loading can elevate the ionic conductivity of the catalyst layers. In addition, the introduction of Nafion into the catalyst layers simultaneously changes the porosity and the gas permeability of the porous layers so that the transport behavior of the gas species is affected.

As Nafion is loaded, the total volume of the catalyst layer (υ_t) may be divided into three major portions, namely, the volume occupied by the solid catalyst particles (υ_S), the volume occupied by Nafion (υ_N), and the volume of the void space (υ_V). The volume fractions of the three portions, appearing in Eqs. (8) and (15), are denoted by $\varepsilon_{S,Cat} = \upsilon_S/\upsilon_t$, $\varepsilon_{N,Cat} = \upsilon_N/\upsilon_t$, and $\varepsilon_{V,Cat} = 1-\varepsilon_{C,Cat}-\varepsilon_{N,Cat}$, respectively.

2.6. Boundary conditions

1. At the inlet, the inlet velocities for the anode gas (hydrogen) and the cathode gas (air) in the gas channel, $V_{a\,in}$ and $V_{c,\,in}$, are fixed at 0.166 and 0.5 m s^{-1}, respectively. The stoichiometries of hydrogen and air corresponding to the inlet velocities are 1.25 and 3.85 at $V = 4.2$ V, respectively. The inlet mass fractions for all the gas species are listed in Table 1. Note that both the hydrogen and the air enter the fuel cell at 100% relative humidity. The flow boundary condition is fixed independent of the cell performance, implying that this is a constant flow operating mode compared to the constant stoichiometry mode.
2. At the outlet, the exit pressure is prescribed to be 101,325 Pa.
3. The width of a module (l_P) is set to be 1 mm. Therefore, for the faces of the solution domain at $x = 0$ and $x = 1$ mm, symmetric boundary conditions for $\vec{U}$, Y, ϕ, and φ are applied.
4. The solid walls of the gas channels on the carbon plates are impermeable, and hence, on the solid walls, $\partial Y_i/\partial n = 0$ and $\vec{U} = 0$.
5. The ionic conduction takes place only inside the catalyst layers and proton exchange membranes, and the protons are not allowed to transfer into other components; therefore, on the faces of the catalyst layers and the membranes the normal gradient of phase potential is assigned to be zero.
6. Since both the gas channels and the membranes are insulators against electrons, at the boundaries of the gas channels and the membranes, the normal gradient of the electric potential (ϕ) vanishes.

This set of conservation equations, along with the property equations, is solved by adopting a finite-volume scheme on structured grids within the framework of the commercial computational fluid dynamics code (CFD-ACE+). The number of control volumes varies from 502,850 to 710,084 to check the grid-independence of the numerical predictions, and the comparison in the average current density has been made based on the results obtained from different grids. It is found that for the case at $V = 4.2$ V, the relative error is within 1.2%. Therefore, typically the grid containing 502,850 control volumes is used to save computation time without loss of accuracy. In computation, the iteration for the solutions for $\vec{U}$, Y, ϕ, and φ progresses until the following convergence criterion is satisfied:

$$|(\Psi^l_{i,j,k} - \Psi^{l-1}_{i,j,k})/\Psi^{l-1}_{i,j,k}| \le 10^{-6} \quad (16)$$

where Ψ represents each of the variables, $\vec{U}$, Y, ϕ, and φ; l is the iteration number; and i, j and k represent the spatial indices for the x-, y- and z-directions, respectively.

The average current density (**I**) of fuel cells is calculated by integrating a local electric current density distribution on the carbon plate surface at $z = 0$ of cell 1 divided by the carbon plate surface area as $\mathbf{I} = 1/A\int_0^A i_s \cdot dA$, where i_s is the local electric current density on the carbon plate surface, and A is the carbon plate surface area.

It is important to note that condensation of water vapor may be critical to the performance of the six-cell stack. Nevertheless, for the present case, experiments show that the water condensation at the cathode side is not severe, compared to the problem of non-evenly distributed channel flow rate at $V = 4.2$ V, even in a long-term operation. This probably may be attributed to the over-stoichiometric operating condition. The stoichiometry of air is set to be 3.85 so that the air stream may definitely help remove the water condensate. Meanwhile, the straight channels might also significantly aid the water condensate removal. However, at a lower stoichiometry, or for other types of channels where the operating voltage is lower, the effects of water condensation vapor will become severe. In that case, assumption (5) may not be valid. On the other hand, the effects of the temperature distribution may play an important role in the condensation and the vaporization of water. Therefore, the temperature field in the fuel cell stack should also be included because the condensation of water vapor is severe. The conditions for the liquid water to exist were investigated extensively by Wang and coworkers [21,22]. Assumptions (5) and (6) can be partially justified with the observation from the experimental and computational works on the two-phase flow in PEMFC of Refs. [21,22].

(a) Experimental apparatus

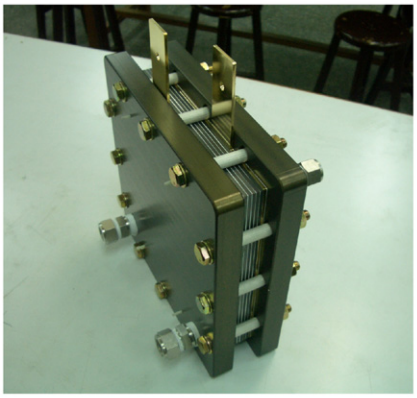

(b) Six-cell stack module (190-W)

Fig. 2. Experimental apparatus and six-cell stack module. (a) Experimental apparatus (b) Six-cell stack module (190 W).

3. Experiments with six-cell PEMFC stack

A six-cell stack (190 W) with cross-sectional area of 22 cm × 22 cm and active area of 14 cm × 14 cm has been installed and tested to partly confirm the present approach's numerical predictions. The purpose of the experiments is simply to test the validity of the commercial code. The operating and geometric conditions in the simulation are consistent with the experimental module. Seven composite graphite plates of 3-mm thickness are used as the bipolar plates. The parallel straight gas channels machined on the bipolar plates are 1 mm wide and 1 mm deep. Six 5-layer membrane exchange assemblies (MEA) provided by Dupont Inc. are placed at the center between two bipolar plates in each cell. The membranes used in this study are Nafion® 112, and the gas diffusion layers are made of carbon fiber papers. Before entering the channels, the fuel and oxidant gases are humidified to maintain 100% relative humidity and 343 K temperature.

In addition, to obtain the polarization curves with the fuel cell, a performance test system has also been set up. In the experiments, the volumetric flow rates of the hydrogen and the air are determined such that the inlet gas velocities agree with the values assigned in the numerical simulation, that is, $V_{a,in} = 0.1667\ \mathrm{m\,s^{-1}}$ and $V_{b,in} = 0.5\ \mathrm{m\,s^{-1}}$. The fuel cell temperature is maintained at 343 K. Photographs of the experimental apparatus and the six-cell stack are shown in Fig. 2.

A comparison between the experiments and the numerical prediction is required for validation of the model. Actually, a number of experiments have been performed for comparison. Herein, only a typical comparison is shown to avoid duplication and for the sake of brevity. The comparison between the numerical predictions and the experimental data for the polarization curves of the six-cell stack module is provided in Fig. 3. Note that the reference current densities, transfer coefficients and reference concentrations have been specified so as to fit the experimental data. It has been observed that the simulation model can be tuned to closely agree with experimental data. In this figure, it is found that at $V = 4.2$ V (average cell voltage is 0.7 V), the numerical and the experimental data are both approximately 2600 A m^{-2}. In this study, the numerical simulation is typically performed for the cases at 4.2 V.

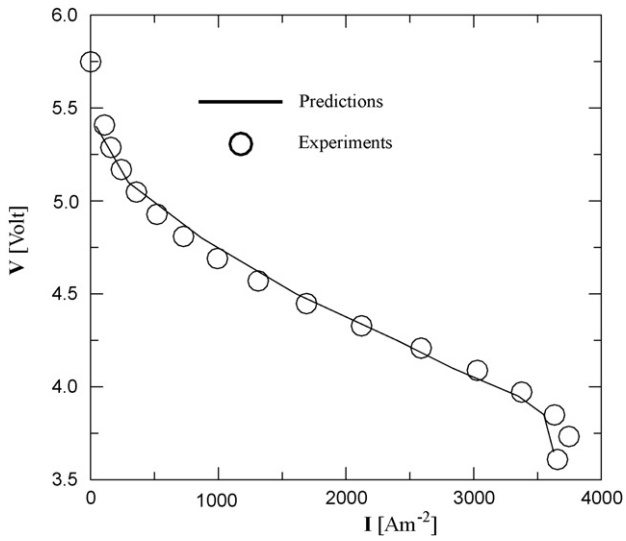

Fig. 3. Polarization curves: comparison between predictions and experiments.

4. Results and discussion

A parametric study of the effects of the channel width ratios (Λ) and the channel heights (h) has been carried out, and a better combination of the size of the gas channels for the individual cells can be determined for evenly distributed cell voltages. In this study, seven test cases with different distributions of channel width ratios and channel heights are investigated, which are listed in Table 2. In this table, Λ_1 to Λ_6 represent the channel width ratios, and h_1 to h_6 the channel heights, for cells 1 to 6, respectively. Among these cases, Case (1) is the base-line case used in the experimental stack system, in which all the sizes of the cells are the equal. In Cases (2) to (7), the sizes of the channels differ in each of the different cells. The relative performance of these cases will be compared with Case (1).

Fig. 4 shows the voltage and the current density distributions at different x–z planes for Case (1). In the case shown in Fig. 4(a),

Table 2
Test cases with different combinations of channel width ratios and channel heights.

	Channel width ratio	Height of gas channel [mm]
Case (1)	$\Lambda_1 = \Lambda_2 = \Lambda_3 = \Lambda_4 = \Lambda_5 = \Lambda_6 = 0.5$	$h_1 = h_2 = h_3 = h_4 = h_5 = h_6 = 1$
Case (2)	$\Lambda_1 = \Lambda_6 = 0.45$, $\Lambda_2 = \Lambda_5 = 0.5$, $\Lambda_3 = \Lambda_4 = 0.55$	$h_1 = h_2 = h_3 = h_4 = h_5 = h_6 = 1$
Case (3)	$\Lambda_1 = \Lambda_6 = 0.4$, $\Lambda_2 = \Lambda_5 = 0.5$, $\Lambda_3 = \Lambda_4 = 0.6$	$h_1 = h_2 = h_3 = h_4 = h_5 = h_6 = 1$
Case (4)	$\Lambda_1 = 0.495$, $\Lambda_2 = 0.500$, $\Lambda_3 = 0.508$ $\Lambda_4 = 0.508$, $\Lambda_5 = 0.502$, $\Lambda_6 = 0.498$	$h_1 = h_2 = h_3 = h_4 = h_5 = h_6 = 1$
Case (5)	$\Lambda_1 = \Lambda_2 = \Lambda_3 = \Lambda_4 = \Lambda_5 = \Lambda_6 = 0.5$	$h_1 = h_6 = 0.95$,$h_2 = h_5 = 1$, $h_3 = h_4 = 1.05$
Case (6)	$\Lambda_1 = \Lambda_2 = \Lambda_3 = \Lambda_4 = \Lambda_5 = \Lambda_6 = 0.5$	$h_1 = h_6 = 0.8$,$h_2 = h_5 = 1$, $h_3 = h_4 = 1.2$
Case (7)	$\Lambda_1 = \Lambda_2 = \Lambda_3 = \Lambda_4 = \Lambda_5 = \Lambda_6 = 0.5$	$h_1 = h_6 = 0.98$, $h_2 = h_5 = 1$, $h_3 = h_4 = 1.02$

the zero voltage is set at the bottom surface of the stack ($V_b = 0$), and the voltage at the top surface (V_t) is assigned to be 4.2 V. It is seen that in the stack, the voltage distribution in the computation domain is decreased from 4.2 to 0 V. On the other hand, the distributions of the current density at each of these same planes exhibit a periodic pattern from cell to cell. However, along the channels, it is observed that the strength of the current density is gradually reduced. This may be attributed to the consumption in the hydrogen and oxygen flowing in the channels that causes a decrease in the local concentrations of the gases downstream.

Mass fraction distributions of oxygen at $x = 0.75$ mm (central cross section on y–z plane on the cathode channels side) for Case (1) at different operating voltages are displayed in Fig. 5. In this figure, cases at $V = 3.6$, 4.2, and 4.8 V are plotted. In general, the highest oxygen concentrations are observed in the inlet manifold area and the lowest in the outlet manifold area. It is found that at $V = 4.8$ V, higher-concentrations of oxygen prevail in the channels of all cells and that the distribution of oxygen concentration is also uniform. However, as the operating voltage is reduced to 3.6 V, the concentration of oxygen in the cells decreases remarkably, and in the downstream zone, the supply of oxygen is obviously insufficient. Furthermore, it is observed that the distribution of mass fraction of oxygen in the cells is uniform at a higher voltage (e.g., 4.8 V); however, at lower voltages, the equality of oxygen concentration in the cells is no longer visible. Note that the more uniform distribution at higher cell voltages results from the constant flow rate operating mode. Since there is much less consumption of reactant gases at lower current densities, the distribution of concentration and thus performance is more uniform. On the other hand, because the reactant flow is kept constant, at a lower voltage (associated with

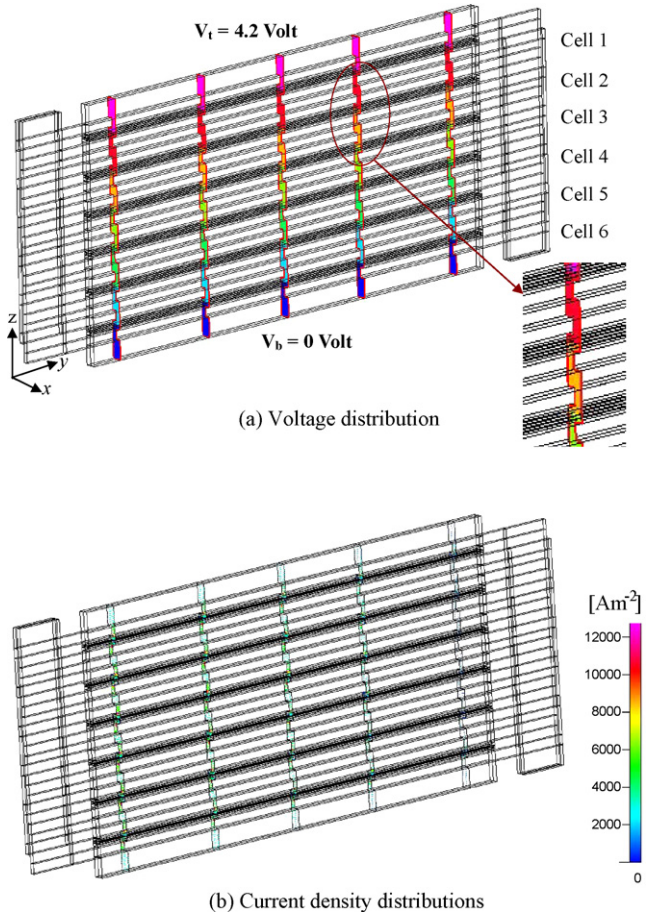

Fig. 4. Voltage and current density distributions at different x–z planes for Case (1).

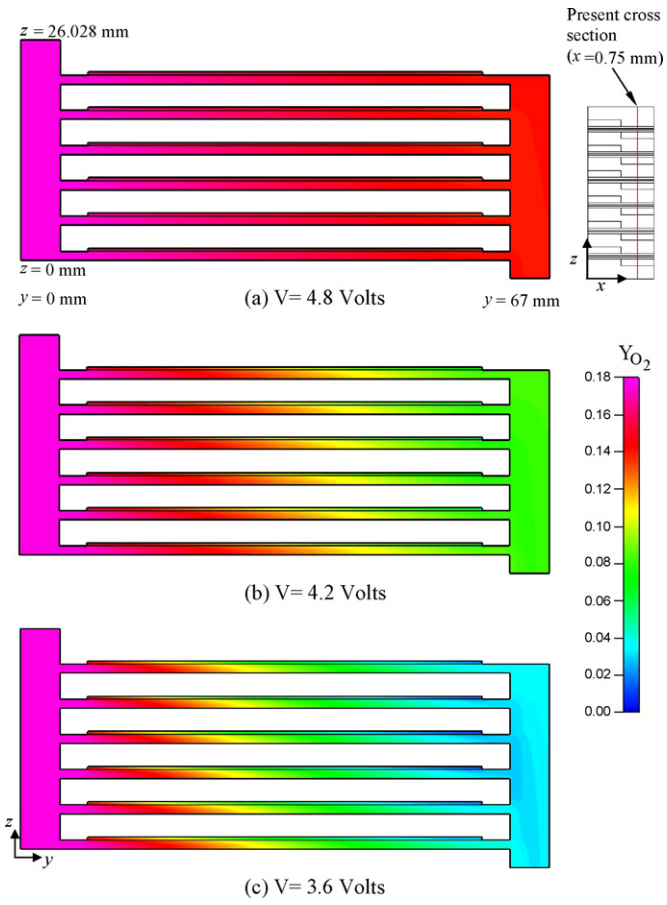

Fig. 5. Mass fraction distributions of oxygen at $x = 0.75$ mm (central cross section on the cathode channels side), for Case (1) at different operating voltages.

higher current densities) it corresponds to a lower stoichiometry situation. Therefore, at lower voltage operations, the oxygen concentration is not uniform. At $V = 3.6$ V, the concentration of oxygen in Cells 3 and 4 is appreciably lower than that in other cells, and Cells 1 and 6 possess highest concentration of oxygen. Also note that the cell voltage results from the gas concentration in the cells. Thus, one may expect that Cells 1 and 6 possess higher cell voltages than Cells 3 and 4. Fig. 6 demonstrates the predicted cell voltages for individual cells of the stack at various operating voltages for Case (1). It is clearly found that the individual cell voltages at $V = 4.8$ V are relatively uniform, whereas at $V = 3.6$ V the individual cell voltages are obviously different for different cells. As expected, Cells 1 and 6 possess higher cell voltages, and Cells 3 and 4 have lower voltages. In accordance with the obtained results, it is recognized that an even voltage distribution results from a uniform reactant gas distribution over the flow fields of the cells. Therefore, in this study, the channel width ratios or the heights of gas channels are adjusted for individual cells to yield a uniform distribution of the reactant gases. It is noted that the sizes of the channels are the same for both the cathode and the anode bipolar plates. Therefore, only the cathode channels sizes are mentioned in the remainder of the paper.

4.1. Adjustment in channel width ratios

As stated in the preceding section, Case (1) has with some disadvantages, and there is still room for significant improvement in the uniformity of cell voltages, especially at lower operating voltage. Therefore, various new design models are further tested in this study by numerical experiments to determine a better design.

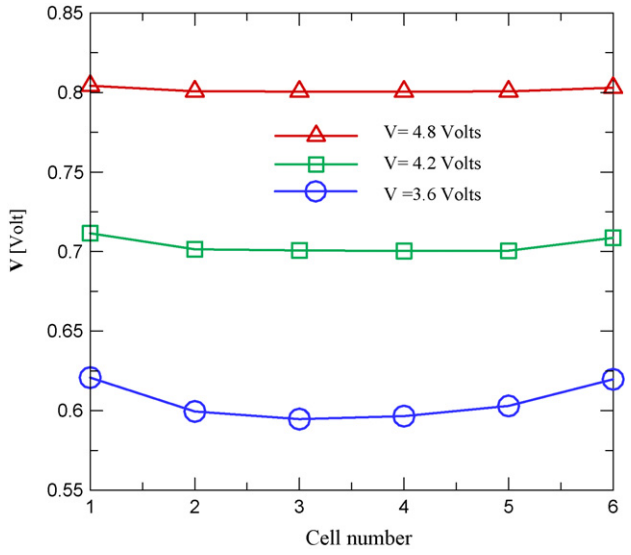

Fig. 6. Cell voltages for individual cells of the stack at various operating voltages, for Case (1).

Figs. 7 and 8 show the mass fraction distributions of oxygen at the same cross section for Case (2) and Case (3), respectively, at different operating voltages. In Case (2), to increase the oxygen concentration in Cells 3 and 4 and decrease the oxygen concentration in Cells 1 and 6, one elevates the channel width ratio of Cells 3 and 4 to be 0.55 and also reduces the width ratio of Cells 1 and 6 to

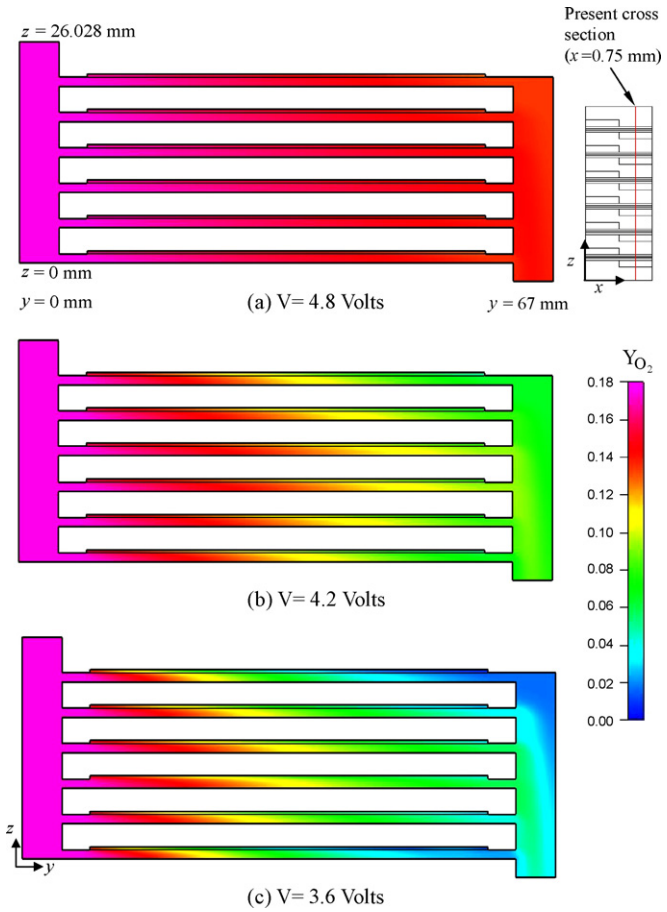

Fig. 7. Mass fraction distributions of oxygen at $x = 0.75$ mm (central cross section on the cathode channels side), for Case (2) at different operating voltages.

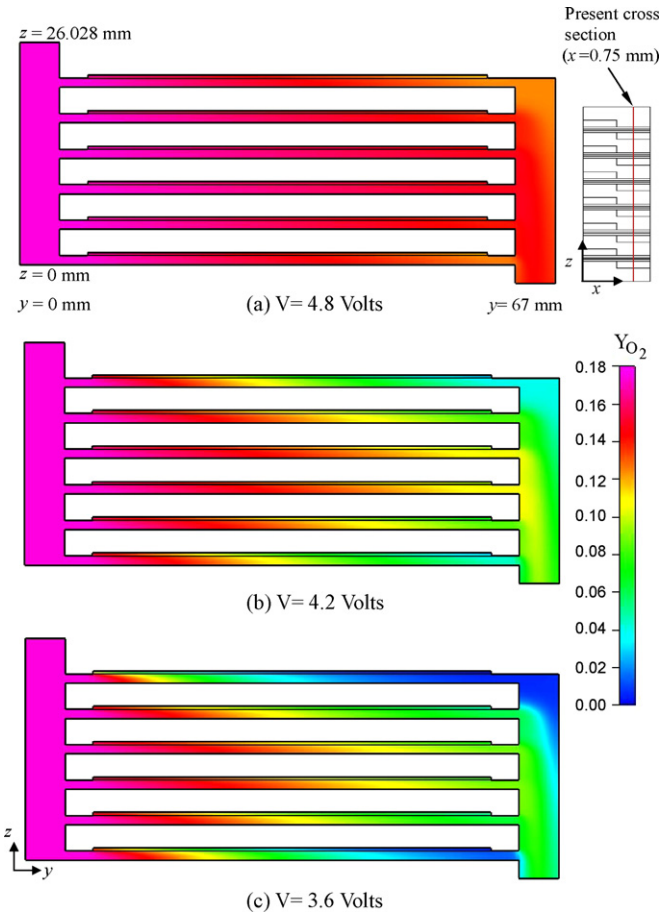

Fig. 8. Mass fraction distributions of oxygen at $x = 0.75$ mm (central cross section on the cathode channels side), for Case (3) at different operating voltages.

be 0.45. Likewise, the flows in Cells 3 and 4 are indeed accelerated, and those in Cells 1 and 6 are retarded. However, contrary to the observations in Case (1), in Case (2) the concentration of oxygen in Cells 3 and 4 becomes higher than that in other cells, and Cells 1 and 6 possess a lower concentration of oxygen. The distribution of oxygen concentration is still not uniform over the flow fields of the cells. In Case (3), the channel width ratio of Cells 3 and 4 is further elevated to 0.6, and that of Cells 1 and 6 is reduced to be 0.4. In Fig. 8, it is seen that in this case the uniformity becomes much poorer and hence not acceptable.

According to the results with Cases (1), (2), and (3), it is reasonable to expect a better design that is a compromise between Cases (1) and (3). Therefore, after a series of computations for various size combinations, the channel width ratios are adjusted to be $\Lambda_1 = 0.495$, $\Lambda_2 = 0.500$, $\Lambda_3 = 0.508$, $\Lambda_4 = 0.508$, $\Lambda_5 = 0.502$, and $\Lambda_6 = 0.498$, while the heights of channels for all cells are maintained at 1 mm. This case is referred to as Case (4) as listed in Table 2. The relative performance of Case (4) is shown in Fig. 9, as compared with Cases (1) and (2). The distributions of average mass fraction of oxygen cross at $y = 28.5$ mm (at middle point of channel length). A comparison of the uniformity of concentration is made for these three cases at a lower operating voltage, 3.6 V. In this figure, it is obvious that the design of Case (4) leads to a more uniform concentration distribution in the cells. Detailed information regarding the concentration distribution in the six cells for Case (4) is presented in Fig. 10. In this figure, distributions of mass fraction of oxygen at the interfaces between membranes and cathode catalyst layers in the six cells for Case (4) are plotted. It is observed that the distributions in the six cells are nearly identical. This means that the

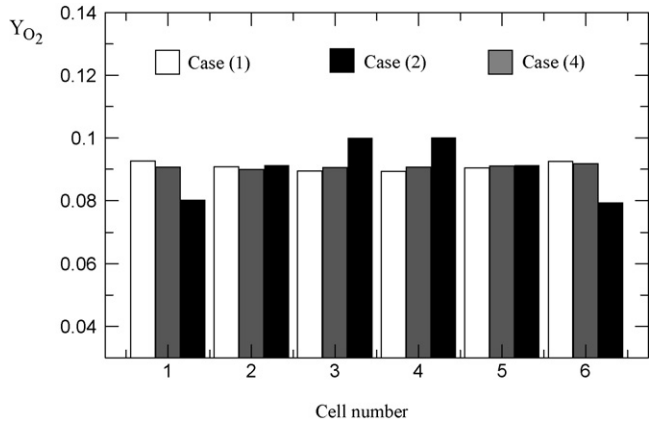

Fig. 9. Distributions of average mass fraction of oxygen on the cross section at $y = 28.5$ mm (at middle point of channel length) in the cells, for Cases (1), (2), and (4) at $V = 3.6$ V.

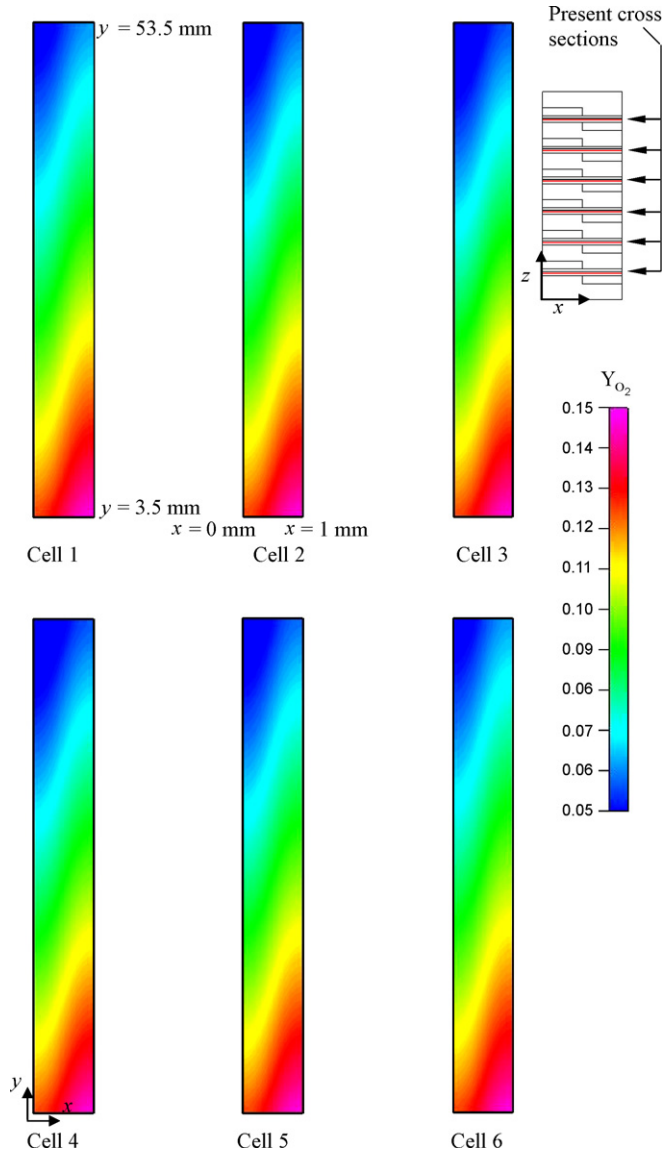

Fig. 10. Distribution of mass fraction of oxygen at the interfaces between membranes and cathode catalyst layers in the six cells for Case (4) at $V = 3.6$ V.

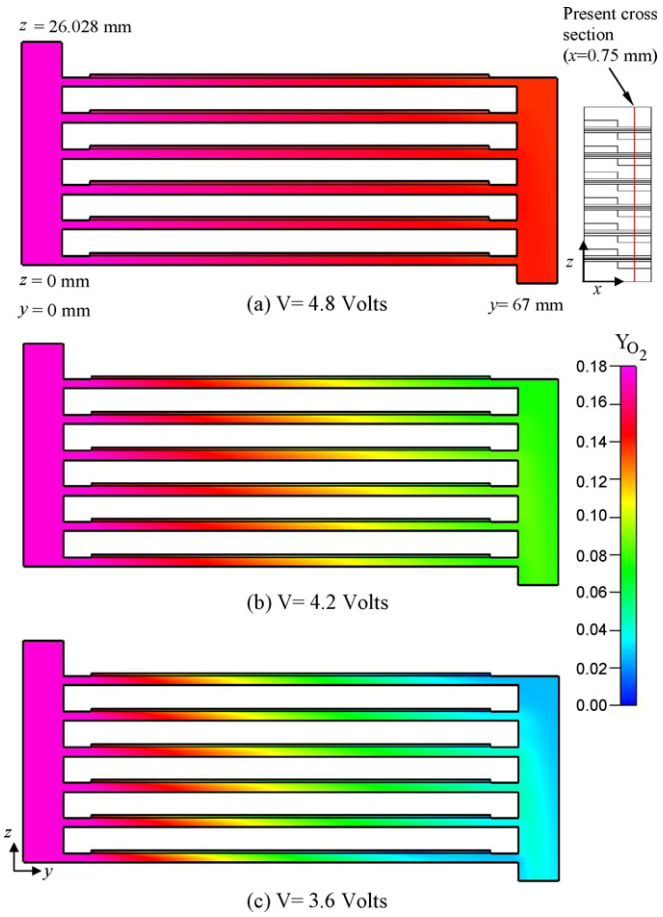

Fig. 11. Mass fraction distributions of oxygen at $x = 0.75$ mm (central cross section on the cathode channels side), for Case (5) at different operating voltages. (a) $V = 4.8$ V (b) $V = 4.2$ V (c) $V = 3.6$ V.

designed manifold is able to supply the reactant gases to the six cells evenly.

It is important to mention that an even distribution of cell voltages is also found with Case (4) when used together with the uniform concentration distribution. As a result, the power density with Case (4) is increased by 16.5% at $V = 4.2$ V ($\mathbf{I} = 3030$ A m^{-2}), as compared to the value with Case (1).

4.2. Adjustment in channel heights

It has been recognized that channel height could be one of the influential geometric parameters on the distribution of the reactant gases in the cells [5,6]. Next, the channel heights in the six cells are adjusted to improve the uniformity of the reactant gas distribution.

Cross-sectional mass fraction distributions of oxygen at $x = 0.75$ mm for Cases (5) and (6) at different operating voltages are displayed in Figs. 11 and 12, respectively. In Case (5), for increasing the oxygen concentration in Cells 3 and 4 and decreasing the oxygen concentration in Cells 1 and 6, the channel heights of Cells 3 and 4 are increased to 1.05 mm, and the channel heights of Cells 1 and 6 are reduced to 0.95 mm. In these two cases, the channel width ratio for all the cells is fixed at 0.5. Fig. 11 shows that, in Case (5), the flows in Cells 3 and 4 are over-accelerated, while those in Cells 1 and 6 are over-retarded. As a result, the concentration of oxygen in Cells 3 and 4 becomes higher than that in other cells, and Cells 1 and 6 now possess lower concentrations of oxygen. This is definitely not the desired situation.

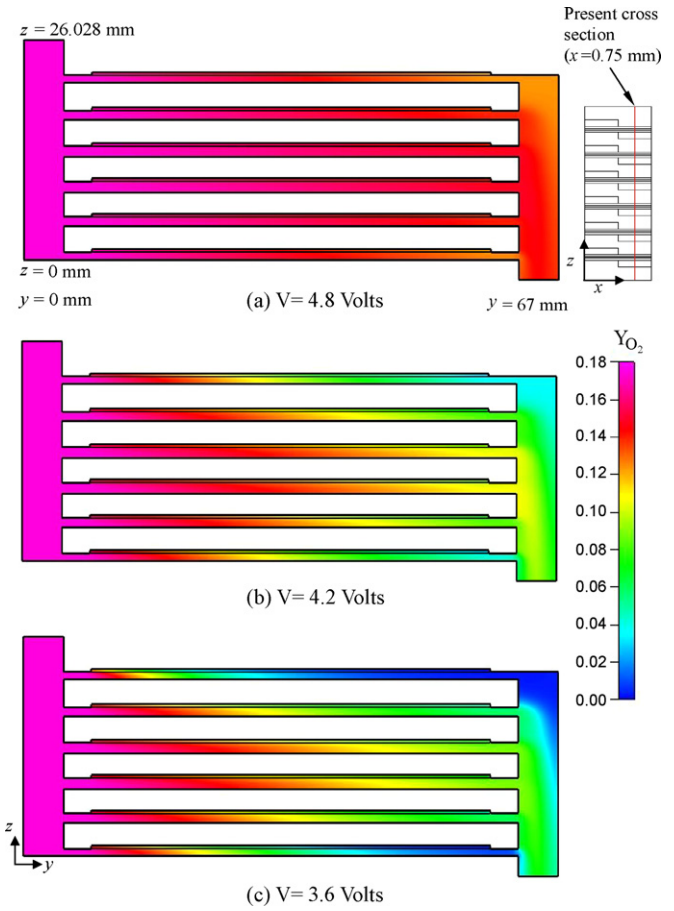

Fig. 12. Mass fraction distributions of oxygen at $x = 0.75$ mm (central cross section on the cathode channels side), for Case (6) at different operating voltages.

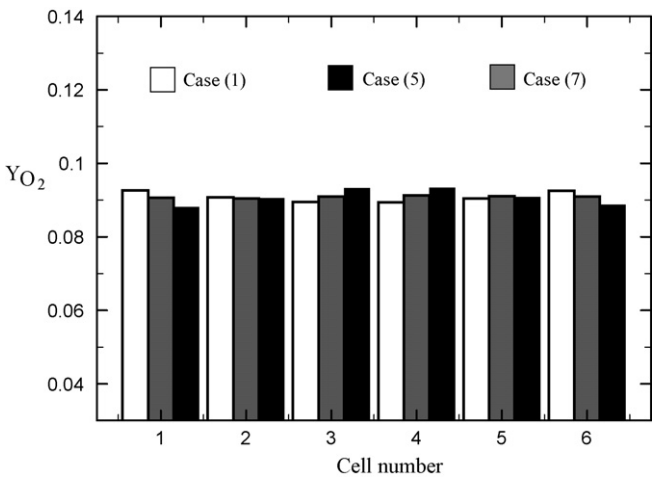

Fig. 13. Distributions of average mass fraction of oxygen on the cross section at $y = 28.5$ mm (at middle point of channel length) in the cells, for Cases (1), (5), and (7) at $V = 3.6$ V.

Table 3
Electric current density at various operating voltages for the test cases.

	Operating voltage (V), V	Electric current density ($\mathbf{I}$), A m^{-2}
Case (1)	3.6	3710
Case (2)	3.6	3153
Case (4)	3.6	4303
Case (1)	4.2	2600
Case (4)	4.2	3030
Case (7)	4.2	2940

Furthermore, considering Case (6) in which the channel heights of Cells 3 and 4 are further elevated to 1.2 mm, and those of Cells 1 and 6 are reduced to be 0.8 mm, one observes in Fig. 12 that the uniformity of gas concentration becomes worse, especially at low operating voltages. For example, at $V = 3.6$ V, the oxygen concentrations in Cells 1 and 6 are rather low, indicating an insufficient oxygen supply for the two cells.

Similarly, the results presented in Figs. 5, 11 and 12 reveal that a better combination for the channel heights for different cells should be a compromise between Cases (1) and (5). Therefore, a series of computations for various size combinations has been carried out in order to determine the best combination for the channel heights for different cells. The suggested design is listed in Table 2 and numbered as Case (7). In Case (7), the channel heights are adjusted to $h_1 = 0.98$ mm, $h_2 = 1.0$ mm, $h_3 = 1.02$ mm, $h_4 = 1.02$ mm, $h_5 = 1.0$ mm, and $h_6 = 0.98$ mm, while the channel width ratio is fixed at 0.5. Fig. 13 conveys the distributions of the average mass fraction of oxygen on the cross section at y = 28.5 mm (at the mid-point of the channel length) in the cells for Cases (1), (5), and (7) at $V = 3.6$ V. In this figure, it is noticed that the design of Case (7) results in a more uniform concentration distribution in the cells. As compared with Case (1), the improvement in gas concentration distribution in the cells with Case (7) results in an increase in the power density by 13% at $V = 4.2$ V ($\mathbf{I} = 2940$ A m^{-2}).

It may be worth mentioning that the optimization of the channel width ratio (and height) distribution is dependent on the manifold design, the physical properties, and the operation parameters. While the size distribution has been found to be optimal for this cell design, this is not a universal distribution for all manifolds or stack designs. Also note that the pressure drop associated with the channel design is an important issue. However, here in the present study while the sizes of some channels are increased, the sizes of some other channels are decreased so that the average channel width and height are kept at $\Lambda = 0.5$ and $h = 1.0$. In addition, in the parallel straight channels, the pressure drop with fluids flowing in the channels is much less compared to other types of channels. Therefore, the variation of pressure drop is not addressed here. Table 3 shows the numerical data for the electric current density at various operating voltages for the test cases. As expected, Case (4) exhibits a relatively higher current density at both $V = 3.6$ and 4.2 V as compared to other test cases, whereas Case (2) leads to a lower current density due to the non-uniform distribution of the reactants in the cells.

5. Concluding remarks

In this study, a numerical simulation of the transport phenomena in a six-cell PEM fuel cell stack has been performed to investigate the possibility of obtaining evenly distributed cell voltages by adjusting the channel width ratios (Λ) or the heights of gas channels (h) of the cells. Meanwhile, a six-cell fuel cell stack (190 W) has been assembled for experiments, and the polarization curves of the stack have been adopted to verify the validity of the numerical solutions.

In the base-line case, Case (1), it is found that at $V = 4.8$ V, higher-concentrations of oxygen prevail in the channels of all the cells, and the distribution of oxygen concentration is also uniform. However, as the operating voltage is reduced to 3.6, or even 2.8 V, the concentration of oxygen in the cells decreases remarkably, and in the downstream zone, the supply of oxygen is obviously insufficient. Furthermore, it is observed that the concentration of oxygen in Cells 3 and 4 is appreciably lower and higher in Cells 1 and 6. Note that under the assumption of no dry out in the cells, an even

voltage distribution can be obtained if the distribution of reactant gas is uniform among the cells. Therefore, in this study, the channel width ratios and the heights of gas channels are adjusted to yield a uniform distribution of the reactant gases in the cells.

Results show that an even distribution in cell voltages can be obtained simply by adjusting the channel width ratios for individual cells. Based on the numerical simulation, it is found that the design of Case (4) leads to a more uniform cell voltage distribution in the cells. In Case (4), the channel width ratios are $\Lambda_1 = 0.495$, $\Lambda_2 = 0.500$, $\Lambda_3 = 0.508$, $\Lambda_4 = 0.508$, $\Lambda_5 = 0.502$, and $\Lambda_6 = 0.498$, while the heights of channels for all cells are maintained at 1 mm. Based on the design of Case (4), the power density is increased by 16.5% at $V = 4.2$ V, as compared to the value with Case (1).

On the other hand, an even distribution in cell voltages can also be obtained by adjusting the channel heights for individual cells. A better combination of the channel heights for individual cells, which is labeled as Case (7), has been found, and the combination is $h_1 = 0.98$ mm, $h_2 = 1.0$ mm, $h_3 = 1.02$ mm, $h_4 = 1.02$ mm, $h_5 = 1.0$ mm, and $h_6 = 0.98$ mm, while the channel width ratio is fixed at 0.5. As compared with Case (1), the improvement in gas concentration distribution in the cells with Case (7) results in an increase in the power density by 13% at $V = 4.2$ V.

Acknowledgements

The authors would like to thank the National Science Council, Taiwan, ROC, for their financial support under Grant: NSC95-2221-E-006-502. The authors would also like to thank Tatung Company for its support in the fuel cell stack experiments.

References

[1] T. Berning, D.M. Lu, N. Djilali, J. Power Sources 106 (2002) 284–294.
[2] S. Dutta, S. Shimpalee, J.W. Van Zee, J. Appl. Electrochem. 30 (2000) 135–146.
[3] G. Hu, J. Fan, S. Chen, Y. Liu, K. Cen, J. Power Sources 136 (2004) 1–9.
[4] L. You, H. Liu, Int. J. Heat Mass Transfer 45 (2002) 2277–2287.
[5] C.H. Cheng, H.H. Lin, G.J. Lai, J. Power Sources 164 (2007) 730–741.
[6] C.H. Cheng, H.H. Lin, G.J. Lai, J. Power Sources 165 (2007) 803–813.
[7] S. Giddey, F.T. Ciacchi, S.P.S. Badwal, J. Power Sources 125 (2004) 155–165.
[8] T.V. Nguyen, M.W. Knobbe, J. Power Sources 114 (2003) 70–79.
[9] M.W. Knobbe, W. He, P.Y. Chong, T.V. Nguyen, J. Power Sources 138 (2004) 94–100.
[10] J. Scholta, N. Berg, P. Wilde, L. Jörissen, J. Garche, J. Power Sources 127 (2004) 206–212.
[11] W.H. Zhu, R.U. Payne, D.R. Cahela, B.J. Tatarchuk, J. Power Sources 128 (2004) 231–238.
[12] I. Mohamed, N. Jenkins, J. Power Sources 131 (2004) 142–146.
[13] X. Yu, B. Zhou, A. Sobiesiak, J. Power Sources 147 (2005) 184–195.
[14] K. Jiao, B. Zhou, P. Quan, J. Power Sources 154 (2006) 124–137.
[15] K. Jiao, B. Zhou, P. Quan, J. Power Sources 157 (2006) 226–243.
[16] Y. Shan, S.Y. Choe, J. Power Sources 158 (2006) 274–286.
[17] G. Karimi, J.J. Baschuk, X. Li, J. Power Sources 147 (2005) 162–177.
[18] M. Pan, Y. Tang, L. Pan, L. Lu, Chem. Eng. J. 137 (2008) 339–346.
[19] O. Tonomura, S. Tanaka, M. Noda, M. Kano, S. Hasebe, I. Hashimoto, Chem. Eng. J. 101 (2004) 397–402.
[20] T.E. Springer, T.A. Zawodzinski, S. Gottesfeld, J. Electrochem. Soc. 138 (1991) 2334–2342.
[21] S. Basu, J. Li, C.Y. Wang, J. Power Sources 187 (2009) 431–443.
[22] I. Hussaini, C.Y. Wang, J. Power Sources 187 (2009) 444–451.